

Article

Genesis of the Koka Gold Deposit in Northwest Eritrea, NE Africa: Constraints from Fluid Inclusions and C–H–O–S Isotopes

Kai Zhao ¹, Huazhou Yao ¹, Jianxiong Wang ¹, Ghebsha Fitwi Ghebretnsae ², Wenshuai Xiang ¹ and Yi-Qu Xiong ^{3,4,*}

¹ Wuhan Center, China Geological Survey (Central South China Innovation Center for Geosciences), Wuhan 430205, China; kabao_8725@163.com (K.Z.); yaohuazhou123@163.com (H.Y.); wangjianxiong00@163.com (J.W.); oldwenzi@163.com (W.X.)

² State Key Laboratory of Geological Processes and Mineral Resources, Faculty of Earth Sciences, China University of Geosciences, Wuhan 430074, China; ohghebsh@gmail.com

³ State Key Laboratory of Geological Processes and Mineral Resources, Faculty of Earth Resources, Collaborative Innovation Center for Exploration of Strategic Mineral Resources, China University of Geosciences, Wuhan 430074, China

⁴ Key Laboratory of Metallogenic Prediction of Nonferrous Metals and Geological Environment Monitoring, Ministry of Education, School of Geosciences and Info-Physics, Central South University, Changsha 410083, China

* Correspondence: xiongyiqu@126.com

Received: 14 January 2019; Accepted: 21 March 2019; Published: 27 March 2019



Abstract: The Koka gold deposit is located in the Elababu shear zone between the Nakfa terrane and the Adobha Abiy terrane, NW Eritrea. Based on a paragenetic study, two main stages of gold mineralization were identified in the Koka gold deposit: (1) an early stage of pyrite–chalcopyrite–sphalerite–galena–gold–quartz vein; and (2) a second stage of pyrite–quartz veins. NaCl–aqueous inclusions, CO₂–rich inclusions, and three-phase CO₂–H₂O inclusions occur in the quartz veins at Koka. The ore-bearing quartz veins formed at 268 °C from NaCl–CO₂–H₂O(–CH₄) fluids averaging 5 wt% NaCl eq. The ore-forming mechanisms include fluid immiscibility during stage I, and mixing with meteoric water during stage II. Oxygen, hydrogen, and carbon isotopes suggest that the ore-forming fluids originated as mixtures of metamorphic water and magmatic water, whereas the sulfur isotope suggests an igneous origin. The features of geology and ore-forming fluid at the Koka deposit are similar to those of orogenic gold deposits, suggesting that the Koka deposit might be an orogenic gold deposit related to granite.

Keywords: C–H–O isotopes; fluid inclusion; Koka deposit; orogenic gold deposit

1. Introduction

The Nubian Shield, located in northeastern Africa, is an important Gondwana metallogenic domain [1,2] that formed during the Neoproterozoic Pan-African orogenic cycle (ca. 900–550 Ma) [2,3]. Most of the Volcanic-associated Massive Sulfide (VMS) type and quartz vein-hosted gold ± sulfide deposits and occurrences in Eritrea are concentrated along NNW- and NNE-trending narrow zones in the south Nubian Shield [4]. Ghebreab et al. [5] named these zones, the Augaro-Adobha Belt (AAB) and the Asmara-Nakfa Belt (ANB). Both the world class Bisha VMS and Koka gold deposits are located in the AAB copper and gold metallogenic belt [6,7].

The Koka gold deposit is located in northwest Eritrea, which has a long mining history that extends back to the Egyptian Pharaohs. However, modern mining began in the early 20th century.

During the Italian colonization, until it was terminated due to the war for independence. Following independence in 1991, several foreign mining companies from China, South Africa, India, Japan, the United Kingdom, Australia, and Canada have been involved in exploring the mineral potential of the country. As a result of several years of explorations, Koka gold still has promising prospects.

Previous studies have suggested that the Koka deposit is a vein-type gold deposit, which is controlled by the shear zone and Koka granite, and is considered to be an orogenic-like gold deposit [8]. However, orogenic gold deposits are commonly unrelated to the granite [9–11], making the genesis of Koka gold deposits enigmatic. The key question is the metal and fluid source, and the evolutionary history of ore-forming fluid.

Therefore, in order to understand the genesis of the Koka deposit, we conducted a detailed study of deposit geology, fluid inclusions (FIs), quartz C–H–O isotopes, and the sulfide S isotope of the Koka gold deposit to better constrain the fluid and metal source, ore-forming fluid evolutionary history, and genesis.

2. Regional Geology

Tectonically, the Koka gold deposit is located in the south Nubian Shield. The shield was formed by the collision between East and West Gondwana upon the closure of the Mozambique Ocean during the Neoproterozoic Pan-African orogenic cycle (ca. 900–550 Ma) (Figure 1a) [3]. The prolonged tectonomagmatic evolution of the Arabian-Nubian Shield involves the rifting and breakup of Rodinia, the formation and accretion of island-arcs, continental collision, extension, and orogenic collapse [2]. Voluminous magmatic activities have also been recorded that are associated with all phases of the tectonic evolution. High strain NNE to NNW trending brittle–ductile shear zones conformable with major fabrics of ANS terranes are dominant in the shield [12]. It is suggested that some of these shear zones that contain dismembered ophiolitic suites represent the major suture zones between terranes [13]. However, others are strike-slip faults and belts of shearing and folding that have modified older sutures [14,15]. Studies have shown that the later types of shear zones are known to host numerous VMS-type polymetallic and orogenic gold deposits and occurrences [15].

More than 60% of the territory of Eritrea is part of the southern Nubian Shield (Figure 1b). The geological setup of the country is made up of three major stratigraphic successions: the basement rocks constituting the Precambrian greenstone volcano-sedimentary assemblages, which are unconformably overlain by Paleozoic and Mesozoic sedimentary and volcanic rocks, which are in turn overlain by sedimentary and volcanic rocks of the Paleogene to Quaternary ages [7]. Based on lithological and structural characteristics, the Eritrean Neoproterozoic basement has been divided into five tectono-stratigraphic terranes: (1) the Barka terrane in the west, mainly composed of upper amphibolite to granulite metasedimentary and mafic gneiss complexes; (2) the Hagar terranes in the north are dominated by oceanic affinity supra-subduction mafic and felsic volcanic rocks; (3) the Adobha Abiy terrane in the central and western parts is principally composed of highly deformed ophiolites and post-accretionary basinal sediments, which are imbricated by the regional shear zones of the Elababu shear zone (ESZ) in the east and the Baden shear zone (BSZ) in the west; (4) the Nakfa terrane occupying more than half of the basement complex contains greenschist facies volcano-sedimentary and syn- to post-collision granitoid rocks; and (5) the easternmost Arig terrane is a narrow belt of high-grade gneiss and syn- to late-tectonic granitoid rocks along the Red Sea lowlands composition [16–18].

Regional structures including the NNW-striking brittle–ductile shear zones and strike-slip faults, low angle thrust faults, fold structures as well as local macroscopic en-echelon quartz veins and tension gashes with a general trend of NNE to NNW are commonly developed on the Precambrian granitoid-greenstone belt. Among these, the ductile strike-slip shear zones are the most prominent tectonic structures in the region and can be traced for several kilometers in length and several meters to several tens of meters in width. The dominantly sinistral AAB and dextral ANB are the two main transpressional strike-slip shear zones, along which the important mineral deposits occur [5]. Semi-brittle shear zones developed synchronously along axial planes of isoclinal folds are also common

structures on the greenschist metamorphic rocks. Syn- to late-tectonic granitoid magmatic rocks intrude along the ductile shear zones as elliptical rigid bodies [5]. These magmatic rocks are dominated by granite, granodiorite, and diorite, and are accompanied by fine-grained rocks, dolerite, and quartz porphyry [7].

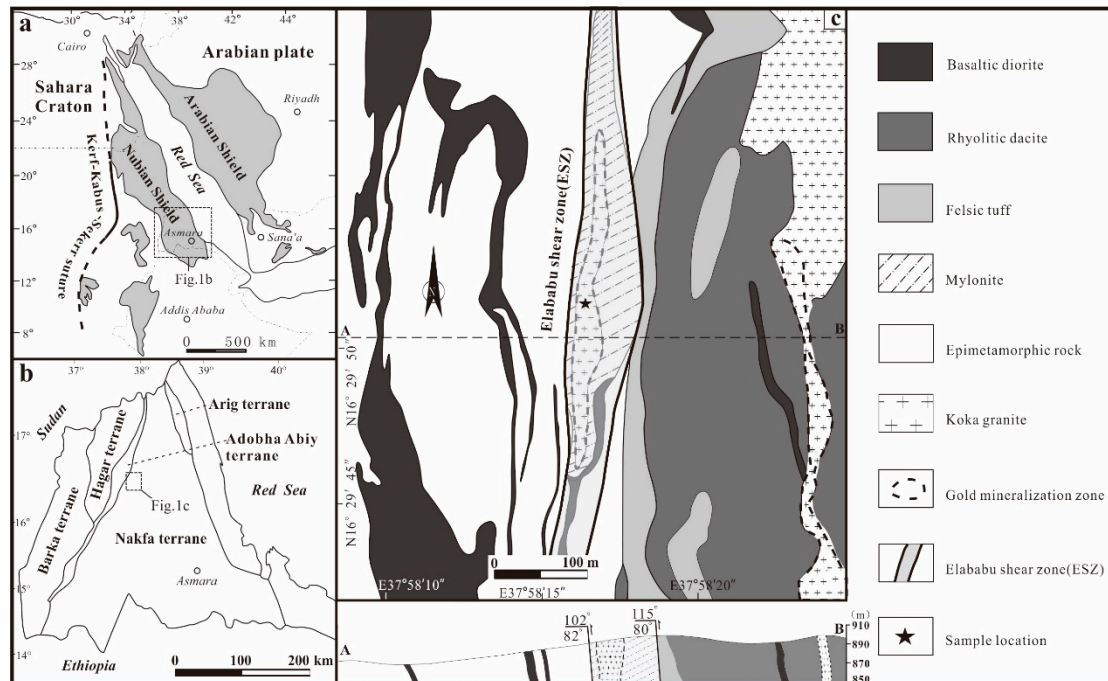


Figure 1. (a) Tectonic scheme of the Koka deposit (after Johnson et al. [15]). (b) Location of the Koka deposit (after Zhao et al. [19]). (c) Geological map of the Koka gold deposit (after Dean et al. [20]).

3. Geology of the Koka Deposit

The Koka gold mine is located in the Elababu shear zone (ESZ) that separates the Nakfa terrane in the east from the Adobha Abiy terrane in the west. The ESZ is the dominant ore- and granite-controlling structure in the area, where the ore bodies are strictly distributed in the SN-striking ESZ. The ESZ is characterized by the occurrence of thrust nappe faults (strike to $10\sim 20^\circ$, tending to the southwest) and low grade metamorphic volcanic-sedimentary rocks upright folds (dip angle of limbs is $75^\circ\sim 90^\circ$) along the different lithologic interfaces. The formation of the ESZ is related to the SN-striking extrusion caused by the collision of the Neo-Proterozoic Gondwana continent. The gold-bearing quartz veins commonly occur as reticular veins, with branching and converging features, and have locally expanded to form lens-shaped bodies (Figure 2a). The granite occurring in the ESZ is characterized by strong mylonitization (Figure 2b,c). Preferred orientation of sericite defined the main foliation anastomosing around rotated K-feldspar porphyroclasts (Figure 2d).

The ores are hosted by a relatively fine to medium grained, gray colored, elongated nearly vertically dipping granitic body. The granitic host rock is dominated by primary minerals of plagioclase, quartz, and subordinate K-feldspar with alteration products dominated by sericite, micro-granular albite, and quartz. The host rock is bounded by greenschist facies metamorphic rocks, consisting of intermediate to felsic volcanic and pyroclastic rocks and post-tectonic granitoids in the east part of the Nakfa terrane and sequence of siliciclastic metasedimentary and metavolcanic rocks including tuffaceous greywacke, sandy mudstone, shales and mafic metabasaltic flows, and associated syn-tectonic granitoid rocks in the west part of the Adobha Abiy terrane (Figure 1c). The area is dominated by the NNE shear zones, which are comprised of a series of asymmetric overturned isocline folds and thrust faults, particularly prevailed on the fine grained volcanic and sedimentary rocks.

The high-angle thrust faults are the main controlling structures for the ore-bearing hydrothermal activities in the mine area.

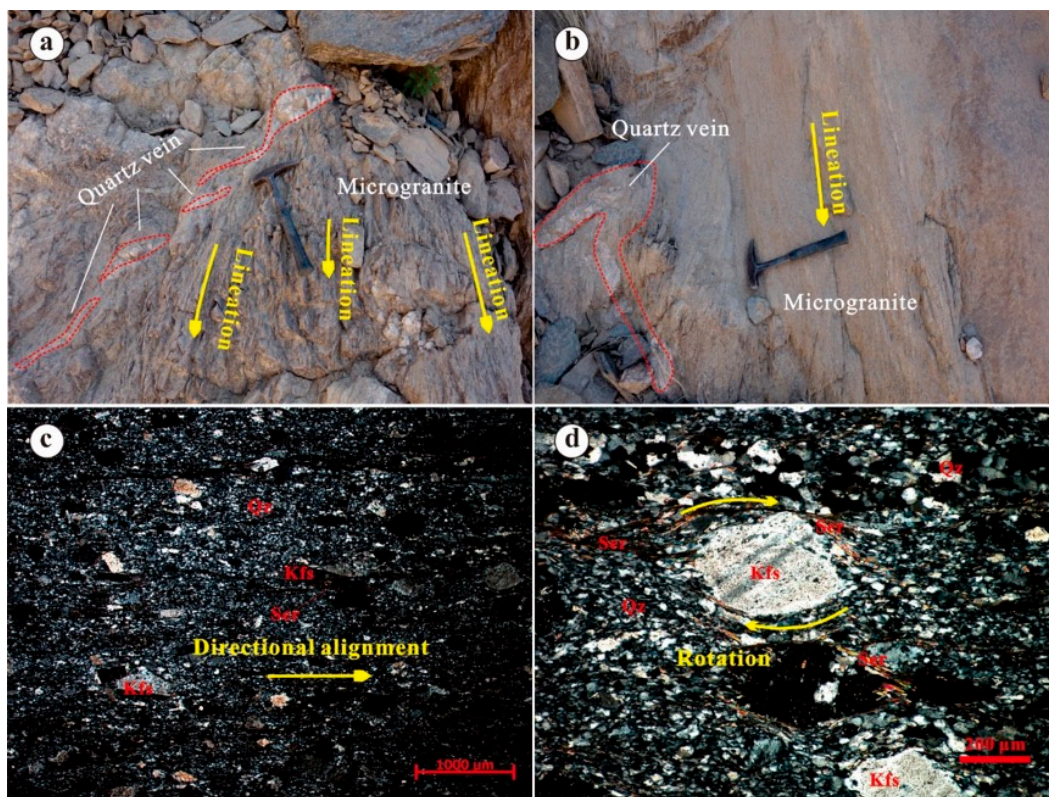


Figure 2. (a) Lens-shaped quartz veins occurring in the microgranite. (b) Microscopic aspects of foliated leucogranite. Foliation is defined by the preferred orientation of sericite. (c) Microscopic view of rotated K-feldspar porphyroclasts with asymmetric strain shadows. (d) Rotation of K-feldspar under microscope. Abbreviations: Kfs = K-feldspar; Qz = quartz; Ser = sericite.

In the Koka gold deposit, the mineralization developed within the relatively competent elongated NNE trending microgranitic body. Post-magmatic deformations have fractured the Koka microgranite (851.2 ± 1.9 Ma, [19]). These tectonic-induced brittle fractures served as a pathway for the gold-bearing hydrothermal fluids and eventually became a mineralized stockworks of quartz veins. The main mineralization zone can be classified into two categories: the quartz vein type and wall-rock alteration type. The former is characterized by intense alteration and the main mineralization zone occurs from 50 to 80 m from the contact of the footwall within the microgranite. This zone is about 10 m wide and is characterized by stockworks of quartz veins with varying widths, generally no more than two meters. The second wall-rock alteration type mineralization mainly developed in the contact zone between the Koka microgranite and footwall metavolcano-sedimentary rocks. As of 2010, the diamond drilling had constrained the Koka gold orebody over a strike length of 650 m, with an average depth of more than 165 m below the surface, and an average grade of about 5–6 g/t, proving that the gold reserves are about 26.13 tons [20].

Gold is mainly formed in quartz veins in the form of native gold. Ore minerals are mainly native gold, pyrite, chalcopyrite, galena, and sphalerite. Gangue minerals are mainly quartz, calcite, and sericite. The types of alterations closely related to gold mineralization are silicification, sericitization, pyrite mineralization, and carbonation and these are superimposed on each other in the mining area and are generally zoning. In particular, silicification is consistent with the main mineralization. Sericitization and pyrite mineralization are beyond the distribution of the mineralization zone, and

formed the sericite + pyrite altered halo boundary. The formation of the carbonation often occurred in the surrounding rock mainly as a carbonated vein, accompanied by other alterations or separately.

Based on microscopic observations, and a paragenetic study of the primary ore mineral assemblages, two main stages of mineralization are recognized in the Koka gold deposit: stage I is characterized by the development of quartz–sulfide–gold veins, of which sulfides are mainly pyrite, chalcopyrite, galena, and sphalerite (Figure 3a). The shape of natural gold is xenomorphic granular and is generally distributed between pyrite and quartz (Figure 3b,c). Pyrites mostly occur as clusters, which are hypautomorphic-cubic crystals with large particle size changes (Figure 3d). Galena is xenomorphic granular in shape and has a distinct triangular cleavage (Figure 3f). Chalcopyrite and sphalerite mostly show a solid solution structure, and aggregates can also be seen, occasionally as a single grain (Figure 3e,g). Stage II is characterized by the development of milky white quartz veins with poor sulfide (Figure 3h). The mineral combination is relatively simple, and only a small amount of its chalcopyrite and fine pyrite can be seen.

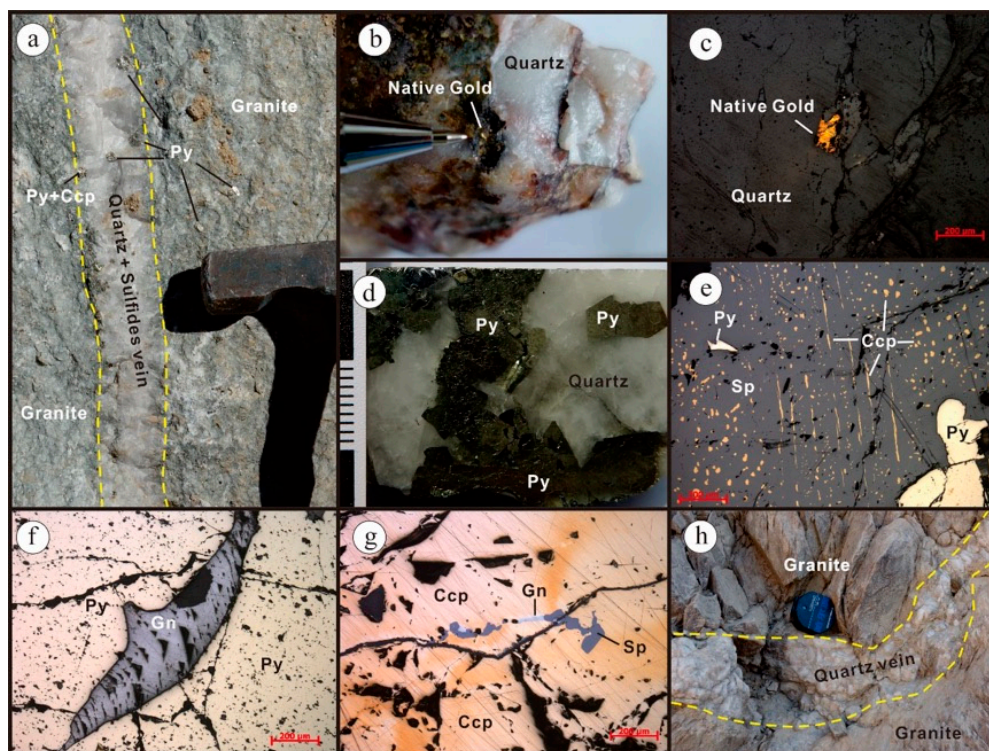


Figure 3. Microscopic photos of the orebodies, hand-specimens, and minerals of the Koka gold deposit. (a) Gold-bearing quartz veins of stage I occur in granite; (b) native gold occurs in quartz veins; (c) native gold occurs in the crack of quartz grains; (d) euhedral pyrite occurs in quartz veins; (e) pyrite coexists with chalcopyrite and sphalerite; (f) pyrite coexists with galena; (g) chalcopyrite coexists with galena and sphalerite; (h) quartz veins of stage II occur in granite. Abbreviations: Ccp = chalcopyrite; Gn = galena; Py = pyrite; Sp = sphalerite.

4. Sampling and Analytical Method

Five ore-bearing quartz samples were collected from the Koka gold deposit, namely KO-15, KO-16, KO-17, KO-3, KO-7, and KO-14. Sampling locations are shown in Figure 1c.

4.1. Fluid Inclusions (FIs)

Fluid inclusion assemblages were characterized prior to the selection of samples for microthermometry. Microthermometry analyses were completed at the Institute of Materials and Engineering, University of Science and Technology Beijing, by using the Linkam THMSG600 heating–

freezing stage (−196 to 600 °C) (Linkam, Surrey, UK). The precision of each measurement was ± 0.1 °C during the cooling cycles and ± 1 °C during the heating cycles. The heating rate was held between 0.2 °C/min and 10 °C/min during these cycles. The temperatures of the phase transitions of the CO₂-bearing fluid inclusions and aqueous inclusions were determined at heating rates of 0.1 °C/min and 0.2 to 0.5 °C/min, respectively. The temperatures of the phase transitions were confirmed by the cycling technique to ensure the accuracy of the microthermometric data. For salinity determination of the CO₂-H₂O FIs, the equation was $S = 15.52022 - 1.02342t - 0.05286t^2$ ($-9.6 \leq t \leq 10$ °C), S = salinity wt% NaCl eqv, t represents the temperature of clathrate in CO₂ FIs [21]. For NaCl-aqueous FIs, the equation was $S = 0.00 + 1.78t - 0.0442t^2 + 0.000557t^3$, $0 < S < 23.3\%$ wt% NaCl eqv, t represents the temperature of ice melting [22].

The chemical composition of the vapor phases in the fluid inclusions was determined by ion and gas chromatography and Raman spectroscopy at the Central South China of the Mineral Resources Supervision and Testing Center, Wuhan. The Raman spectroscopy instrument was a Renishaw inVia, UK. The spectrum ranged from 50 cm^{−1} to 4500 cm^{−1}. The operating conditions included a laser wavelength of 514.5 nm and laser power of 30 mW. The Raman shift was calibrated using a single crystal of silicon. The cation test instrument in the liquid phase composition of the group inclusions was a Hitachi Z-2300 (Hitachi, Tokyo, Japan), and a DIONEX ICS-3000 (Dionex, Sunnyvale, CA, USA) was used for ion chromatography. A GC-2014C was used for gas chromatography. The bursting temperature of the inclusions ranged from 100 to 550 °C, and the precision was 0.01 mg/L (0.01 µg/g).

4.2. Stable Isotope Analytical Methods

The H–O–C isotope analyses were accomplished with a MAT253 mass spectrometer (Finnigan, San Jose, CA, USA) at the Analytical Laboratory of the Beijing Research Institute of Uranium Geology. The accuracy of the O isotope analysis was better than $\pm 0.2\%$, and that of the H isotope analysis was better than $\pm 2\%$, and that of the C isotope analysis was typically better than $\pm 0.1\%$. The amount of O in quartz water (aquartz water) was calculated from the O isotope level of the analyzed quartz by using the fractionation equation $1000\ln\alpha_{\text{quartz water}} = (3.38 \times 10^6)T^{-2} - 3.40$, where T is the temperature in Kelvin [23], and the average fluid inclusion temperature of each stage was used to calculate the $\delta^{18}\text{O}_{\text{water}}$ value.

5. Fluid Inclusions

5.1. Fluid Inclusion Petrography

Fluid inclusions (FIs) of the Koka gold deposit are found in quartz. Quartz is mainly characterized by ductile deformation (quartz). A large number of fluid inclusions including primary, pseudosecondary, and secondary fluid inclusions [22,24] were identified in two mineralization stages of quartz using detailed petrographic observations. Primary and pseudosecondary inclusions occur in the growth zone of quartz (Figure 4), or are distributed as an isolated form. The microthermometric data in this study were basically from primary and pseudosecondary inclusions, and inclusions with only an aqueous liquid phase are the result of necking phenomena and cannot be used for microthermometry. In accordance with the classification principles of Roedder [24] and Lu et al. [22], vapor-to-liquid ratios at room temperature, heating–freezing behaviors, and results of laser Raman analysis were used to classify the fluid inclusions found in the Koka deposit into four types:

(1) Type I, liquid-rich aqueous fluid inclusions ($L_{\text{H}_2\text{O}} + V_{\text{H}_2\text{O}}$), are mainly found in stage II, and are rarely found in stage I. Type I FIs are dominantly liquid-rich inclusions with few pure liquid inclusions. The liquid-rich inclusions have ellipsoidal or irregular shapes with long axes of 8–16 µm and a 75–95 vol% liquid phase. These types of FIs are mostly primary and pseudosecondary inclusions that are distributed in isolation or along the crystal growth (Figure 4a,b).

(2) Type II, CO₂-rich fluid inclusions ($L_{\text{CO}_2} + V_{\text{CO}_2}$), are mainly found in the early stage quartz veins. Liquid-rich CO₂ inclusions have ellipsoidal or irregular shapes with long axes of 6–16 µm

(Figure 4c–f) and a 40–95 vol% liquid phase. Type II FIs dominantly occurred as a liquid phase in room temperature (25 °C), whereas few occurred as two phases. Liquid-rich CO₂ inclusions will appear as vapor in the cooling process. Type II FIs commonly coexist with Type III FIs, and few coexist with Type I FIs (Figure 4d).

(3) Type III, three-phase CO₂-rich fluid inclusions (V_{CO2} + L_{CO2} + L_{H2O}) at room temperature, occurred in both the early and late stages, have ellipsoidal or irregular shapes with long axes of 6–24 μm (Figure 4a,g,h) and a 20–85 vol% liquid phase.

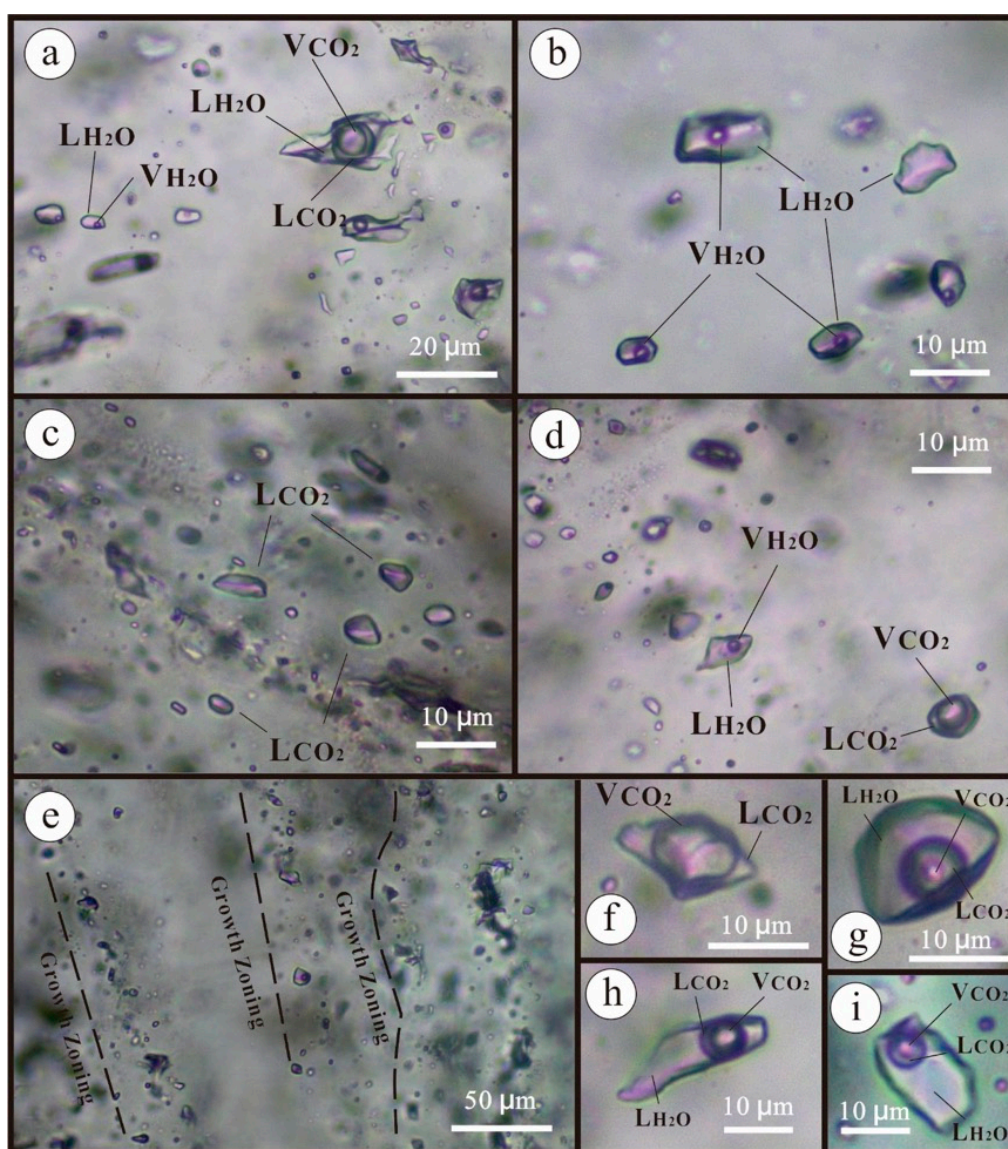


Figure 4. (a) Type I fluid inclusions (FIs) coexist with type III FIs in stage I veins; (b) Type I FIs occur in stage II veins; (c) Abundant Type II FIs occur in stage I veins; (d) Type I FIs coexist with type II FIs in stage I veins; (e) Primary FIs distributed along the crystal growth bands; (f) Type II of vapor-rich FI in stage I; (g) Type II of liquid-rich FI in stage I; (h) Type III FI in stage I; and (i) Type III FI in stage II.

5.2. Fluid Inclusion Microthermometry

Five ore-bearing quartz samples from the Koka gold deposit were selected for ice melting and homogenization temperatures analysis, namely KO-15, KO-16, KO-17, KO-3, KO-7, and KO-14. A total of 135 microthermometric data of all types of fluid inclusions are listed in Table 1 and Figure 5.

Table 1. Summary of microthermometric data of the fluid inclusions from the Koka gold deposit.

Sample No.	Stage	FI type	Size (μm)	Number	T _m , CO ₂ (°C)	T _m , ice (°C)	T _m , Cl (°C)	Th, CO ₂ (°C)	Th, (°C)	Salinity (wt% NaCl)	Density (g/cm ³)
KO-15		Type I, minor	6~12	4		-4.3~-2.4			254~341 (V)	4.0~6.9	0.757~0.822
		Type II, abundant	8~16	9	-56.9~-58.0			-2.3~17.2			0.801~0.904
		Type III, abundant	8~16	11	-56.7~-57.9		5.7~7.8	19.2~30.1	280~356 (V)	4.3~7.9	0.576~0.793
KO-16	Stage I	Type I, minor	6~12	5		-2.6~-1.9			243~288 (V)	3.2~4.3	0.711~0.831
		Type II, abundant	6~12	10	-56.7~-58.2			-4.9~18.9			0.757~0.898
		Type III, minor	6~20	14	-56.8~-58.1		5.8~7.9	19.9~29.6	235~295 (V)	4.1~7.7	0.608~0.783
KO-17		Type I, minor	6~12	6		-3.2~-1.8			223~275 (V)	3.1~5.3	0.783~0.858
		Type II, abundant	6~14	13	-56.8~-58.0			-4.7~16.4			0.812~0.901
		Type III, abundant	10~24	14	-56.6~-58.0		5.3~8.0	10.6~29.4	238~305 (V)	3.3~8.5	0.613~0.862
KO-3		Type I, abundant	8~16	6		-2.6~-1.5			221~288 (V)	2.6~4.3	0.765~0.872
		Type III, abundant	8~20	11	-57.0~-57.9		6.2~8.2	19.7~29.7	228~295 (V)	3.5~7.1	0.613~0.787
KO-7	Stage II	Type I, abundant	8~12	6		-2.8~-1.3			212~280 (V)	2.2~4.7	0.763~0.871
		Type III, abundant	8~24	11	-56.9~-57.4		6.6~8.5	18.5~29.7	232~318 (V)	3.0~7.5	0.597~0.793
KO-14		Type I, minor	8~14	5		-2.6~-0.9			235~267 (V)	2.2~4.3	0.786~0.842
		Type III, abundant	10~22	10	-56.7~-57.3		5.6~8.0	18.2~25.7	259~309 (V)	3.9~8.0	0.672~0.701

(1) Stage I

The fluid inclusions in stage I included types I, II, and III. Type I FIs homogenized to the liquid phase at temperatures ranging from 254 °C to 341 °C, predominantly at 260–280 °C. Their ice melting temperatures ranged from −4.3 °C to −1.8 °C, corresponding to salinities of 3.1–6.9 wt% NaCl eqv, with most around 3–4 wt% NaCl eqv. Type II fluid inclusions showed that the CO₂ phase melting temperatures ranged from −56.7 °C to −58.2 °C, with a peak at −57 °C, and the homogenization temperatures to the liquid phase were −4.9 °C to 18.9 °C. Type III (CO₂-rich) inclusions formed solid CO₂ upon cooling. The solid CO₂ melted at temperatures between −56.6 °C and −58.1 °C, lower than the triple point temperature of pure CO₂ (−56.6 °C). The CO₂-clathrate melting temperatures varied from 5.3 °C to 8.0 °C, corresponding to salinities of 3.3–8.5 wt% NaCl eqv, with most around 6–7 wt% NaCl eqv. Vapor- and liquid-CO₂ homogenized to the vapor phase at temperatures between 10.6 °C and 30.1 °C, higher than the type II FIs in stage I (Figure 6). The total homogenization temperatures of type III inclusions ranged from 235 °C to 356 °C, with most around 280–300 °C.

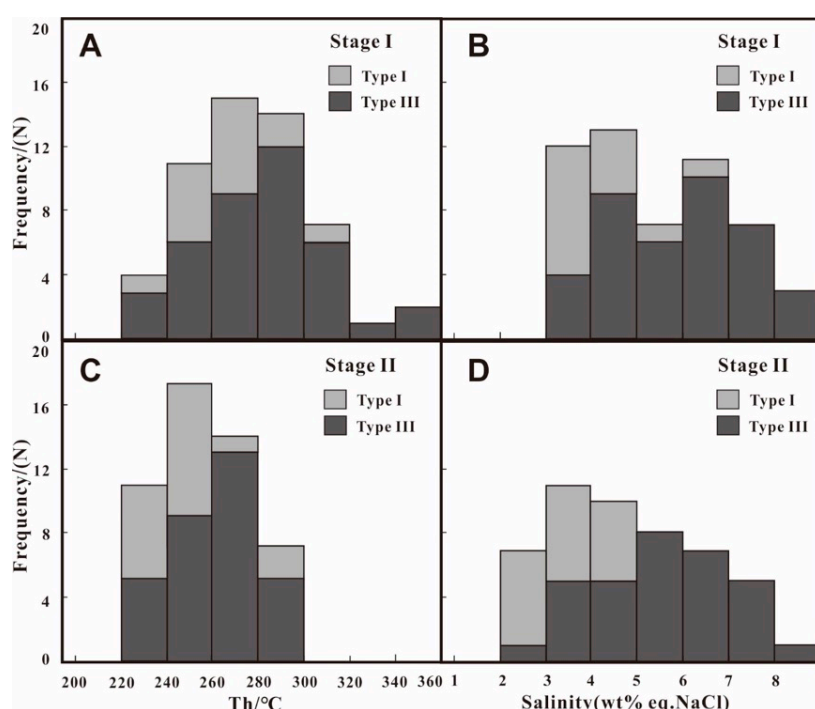


Figure 5. (A,C) Homogenization temperature of different stages of the Koka gold deposit; (B,D) Salinity of different stages of the Koka gold deposit.

(2) Stage II

The fluid inclusions in stage II included types I, III, and rare type II, and the inclusions of type III are commonly vapor-rich ($V/(V + L) > 40\%$). The FIs of type I are dominantly liquid-rich, and homogenized to the liquid phase at temperatures varying from 212 °C to 288 °C, predominantly at 260–280 °C. Their ice melting temperatures ranged from −2.8 °C to −0.9 °C, corresponding to salinities of 2.2–4.7 wt% NaCl eqv, with most around 3–4 wt% NaCl eqv. Type II fluid inclusions showed the CO₂ phase melting temperatures ranged from −56.9 °C to −57.9 °C, and the homogenization temperatures to the liquid phase of 6.8 °C to 17.3 °C. The solid CO₂ of type III inclusions melted at temperatures between −56.9 °C and −57.9 °C, and the CO₂-clathrate melting temperatures varied from 6.2 °C to 8.5 °C, corresponding to salinities of 3.0–8.0 wt% NaCl eqv, with most around 5–7 wt% NaCl eqv. Vapor- and liquid-CO₂ homogenized to the liquid phase at temperatures between 18.5 °C and 29.7 °C, and the total homogenization temperatures of type III inclusions ranged from 232 °C to 318 °C, with most around 260–280 °C.

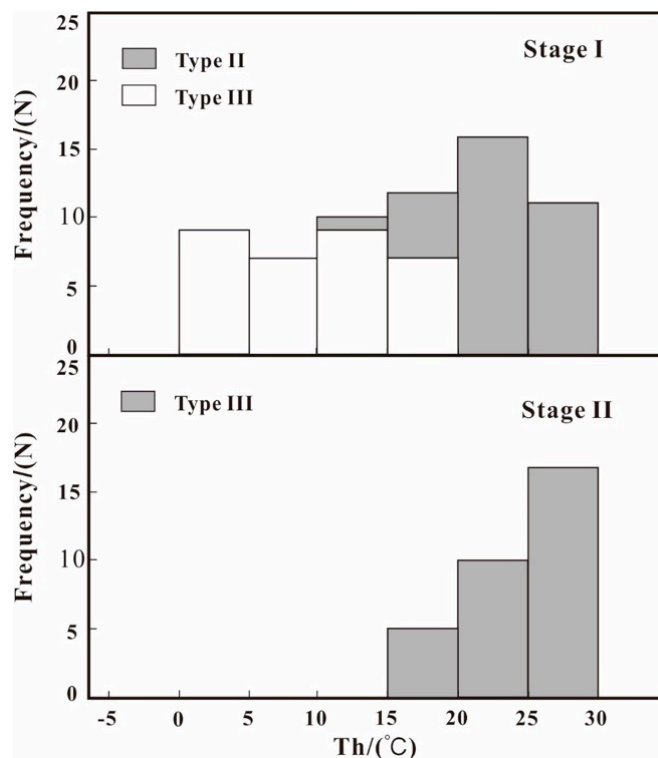


Figure 6. Homogenization temperature of the vapor phase CO₂ in different stages of the Koka gold deposit.

5.3. Laser Raman Spectroscopy

Selected samples based on the fluid inclusion petrology of the two stages were examined by laser Raman micro spectroscopy. The results showed that the composition of FIs in type I was relatively simple, dominated by H₂O (Figure 7d). The composition of type II FIs was basically pure CO₂ (Figure 7c). The inclusion gas of type III was dominated by CO₂ and H₂O, and the aqueous phase also contained some CO₂ (Figure 7a,b).

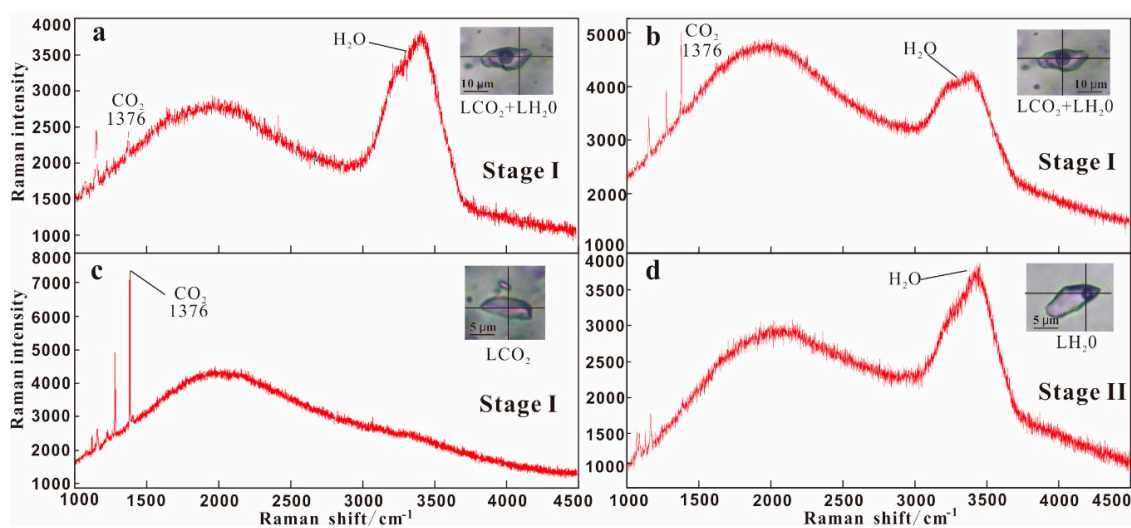


Figure 7. Raman spectra of the fluid inclusion of the Koka gold deposit. (a,b) Type III FI of stage I; (c) Type II FI of stage I; (d) Type I FI of stage II.

5.4. Ion and Gas Chromatography

The results of the composition of the fluid inclusions cluster in quartz based on ion and gas chromatography showed that CO₂ and H₂O were the dominant gaseous ingredients, and CH₄ was rare (Table 2). The average mole% of H₂O and CO₂ of stage I were 0.535 and 0.465, respectively, whereas the average mole% of H₂O increased to 0.753, and the average mole% of CO₂ reduced to 0.245 in stage II. Only 0.11 mole% of CH₄ was detected in sample KO-16 of stage I. The mole% of CO and H₂ of all of the samples were below the detection limit.

The results of the ion chromatography showed that Na⁺ was the dominant cation in both stages, with minor K⁺ and Ca⁺, and the ratio of Na⁺/K⁺ ranged from 20.13 to 26.33, and 12.75 to 17.15, respectively. The anion of the two stages was mainly Cl⁻ with minor SO₄²⁻, and the ratio of Cl⁻/SO₄²⁻ ranged from 11.52 to 17.42, and 19.24 to 31.26, respectively. Moreover, the average content of Na⁺ and Cl⁻ in stage I was 5.40 mg/L and 6.96 mg/L, respectively. Compared with stage I, the average contents of Na⁺ and Cl⁻ in stage II were 9.64 mg/L and 12.63 mg/L, respectively, higher than those in stage I. Li⁺, F⁻, and Br⁻ of all samples are below the detection limit.

Table 2. Results of the ion and gas chromatography of the fluid inclusions from the Koka gold deposit.

Sample No.	Stage	H ₂ O mol%	CO ₂ mol%	CO mol%	CH ₄ mol%	K ⁺ mg/L	Na ⁺ mg/L	Ca ²⁺ mg/L	Mg ²⁺ mg/L	Cl ⁻ mg/L	SO ₄ ²⁻ mg/L
KO-15	Stage I	0.595	0.405	<0.01	<0.01	0.18	4.74	0.09	0.02	5.99	0.52
KO-16		0.526	0.474	<0.01	0.11	0.31	6.24	0.07	<0.01	8.36	0.48
KO-17		0.484	0.516	<0.01	<0.01	<0.01	5.22	0.06	<0.01	6.52	0.56
KO-3	Stage II	0.741	0.259	<0.01	<0.01	0.47	8.06	0.08	<0.01	9.62	0.50
KO-7		0.765	0.235	<0.01	<0.01	0.88	11.22	0.10	0.02	15.63	0.50

6. C–H–O–S Isotopes

The carbon and oxygen isotopic data are listed in Table 3 and plotted in Figure 8. Three quartz samples from the early stage provided δ¹³C value ranging from −5.5‰ to −5.0‰, and the δ¹⁸O value ranged from +9.0‰ to +9.7‰. The δ¹³C and δ¹⁸O values of two quartz samples from the late stage fell within a range of −4.4‰ and +10.1‰ to +10.8‰, respectively.

Table 3. The oxygen, hydrogen, and carbon isotopic compositions of quartz from the Koka gold deposit.

Sample NO.	Stage	Mineral	δD _{smow} (‰)	δ ¹⁸ O _{smow} (‰)	δ ¹⁸ O _{H₂O} (‰)	δ ¹³ C _{v-PDB} (‰)	Temperature (°C)
KO-15	Stage I	Quartz	−52.5	9.7	2.4	−5.0	290
KO-16		Quartz	−57.0	9.0	1.7	−5.4	290
KO-17		Quartz	−50.1	9.5	2.2	−5.5	290
KO-3	Stage II	Quartz	−53.1	10.8	2.7	−4.4	270
KO-7		Quartz	−54.1	10.1	2.0	−4.4	270

The oxygen and hydrogen isotopic data are listed in Table 3 and plotted in Figure 9. The measured δ¹⁸O values of five quartz samples in the two stages ranged from +8.0 to +8.8‰. The δ¹⁸O values of hydrothermal fluids were calculated using the equation of Clayton et al. [21], $1000 \ln a_{\text{quartz-water}} = 3.38 \times 10^6 \times T^{-2} - 3.40$, together with the measured δ¹⁸O_{quartz} values and the corresponding average homogenization temperatures of the FIs in the same stage of the same sample (Table 3). As a result, the δ¹⁸O_{H₂O} values from the early stage and the late stage were +1.7‰ to +2.4‰, and 2.0‰ to +2.7‰, respectively. All samples selected for δ¹⁸O analysis were also analyzed for their hydrogen isotopic composition. The δD_{H₂O} values of the quartz samples in the early stage and the late stage were −57.0‰ to −50.1‰, and −54.1‰ to −53.1‰, respectively.

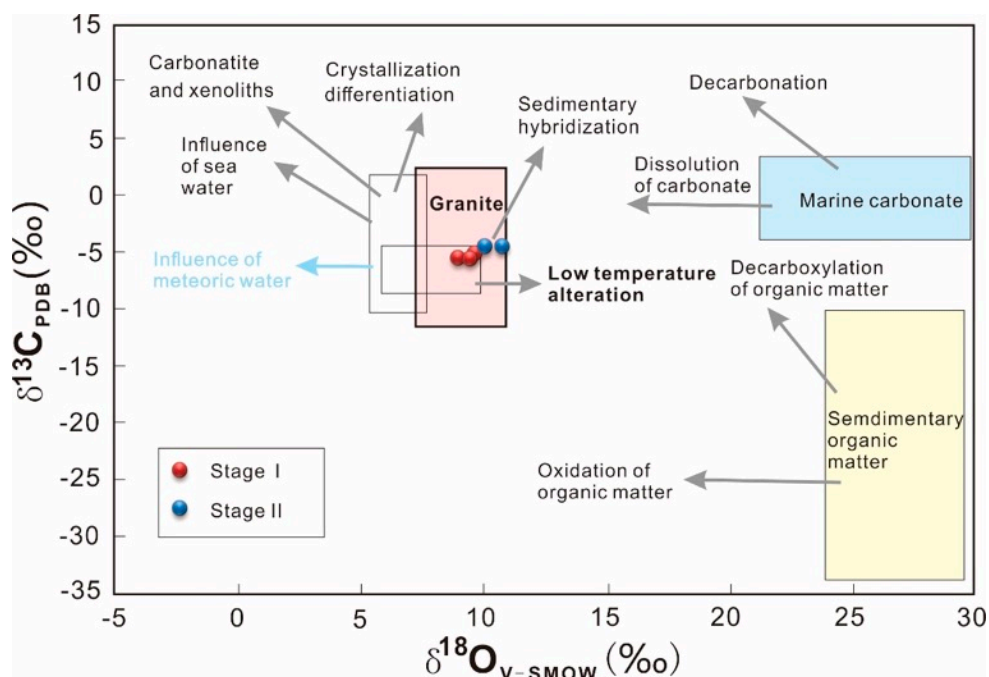


Figure 8. Calculated $\delta^{13}\text{C}$ and $\delta^{18}\text{O}$ values of fluids at Koka (after Chen et al., 2012 [25]).

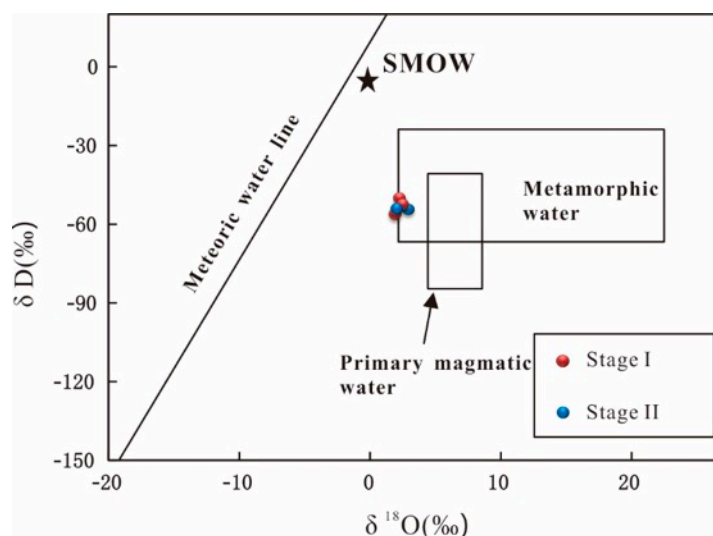
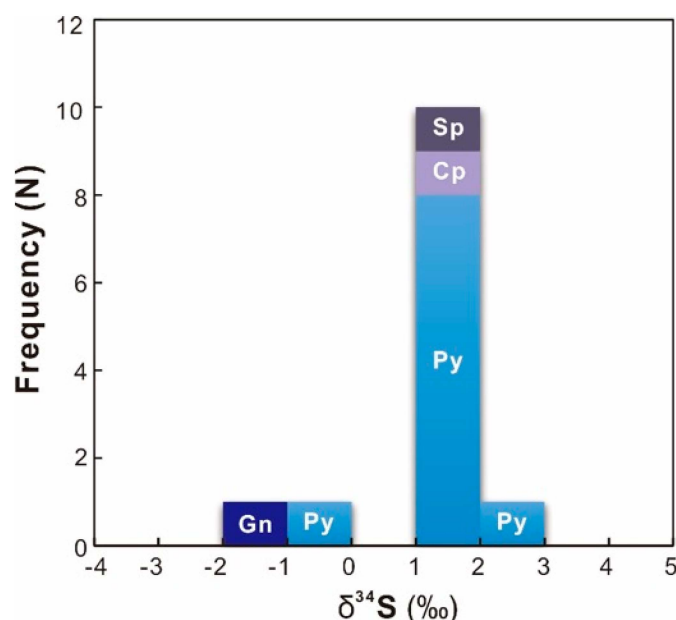


Figure 9. The $\delta^{18}\text{O}$ and δD values of the ore fluids at the Koka deposit. The metamorphic water field, primary magmatic water field, and meteoric water line are from Taylor (1974) [26].

The sulfur isotopic data are shown in Table 4 and plotted in Figure 10. The $\delta^{34}\text{S}$ values of ten pyrite samples from the Koka gold deposit ranged from -0.1‰ to $+2.7\text{‰}$, with an average of $+1.6\text{‰}$, and the $\delta^{34}\text{S}$ value of the samples of one chalcopyrite, one galena, and one sphalerite were $+1.3\text{‰}$, -1.3‰ , and $+1.2\text{‰}$, respectively. Therefore, the sulfur isotopic compositions in the Koka gold deposit showed a relatively narrow range (-1.3 to $+2.7\text{‰}$, around zero), indicating a homogenous sulfur source.

Table 4. Sulfur isotopic compositions of sulfides from the Koka gold deposit.

Sample No.	Stage	Mineral	$\delta^{34}\text{S}_{\text{CDT}}$ (‰)
KO-11		Pyrite	1.7
KO-11		Pyrite	−0.1
KO-15		Pyrite	1.3
KO-16		Pyrite	1.4
KO-17	Stage I	Pyrite	1.6
KO-17		Pyrite	1.6
KO-17		Chalcopyrite	1.3
KO-17		Galena	−1.3
KO-17		Sphalerite	1.2
KO-3	Stage II	Pyrite	1.9
KO-3		Pyrite	1.9
KO-7		Pyrite	2.7
KO-14		Pyrite	1.8

**Figure 10.** Histograms of the $\delta^{34}\text{S}$ values of sulfide for the Koka deposit.

7. Discussion

7.1. Nature and Evolution of Ore-Forming Fluid

CO_2 -bearing FIs were the most abundant occurrence in the Koka gold deposit, with moderate liquid-rich aqueous FIs. Generally, the results of fluid inclusion petrography, microthermometry, and laser Raman micro-spectroscopy showed that the ore-forming fluid of the Koka gold deposit was a medium- to low-temperature and low-salinity CO_2 - NaCl - H_2O system.

(1) Stage I

The ore-forming fluid of this stage was a medium-temperature, low-salinity NaCl - H_2O - CO_2 (- CH_4) fluid (CH_4 was detected via gas chromatography). The majority of CO_2 and CH_4 are likely to be from the metamorphic strata [10,27–29]. Fluid immiscibility is one of the dominant ore-forming mechanisms in gold deposits [30–32]. The common coexistence of type I and II FIs during stage I suggests that they were entrapped simultaneously, and homogenized in different ways, which suggests that fluid immiscibility occurred prior to their entrapment [33]. The plot of salinity vs. the homogenization temperatures (Figure 11) indicates that the ore-forming fluid underwent a fluid

immiscibility process during stage I at Xiangdong (three-phase CO₂-rich inclusions commonly coexist with two-phase aqueous inclusions in quartz, with similar homogenization temperatures [24]), which is likely to be due to the decrease in temperature and pressure as the ore-forming fluid ascended, leading to the escape of CO₂ from the fluid.

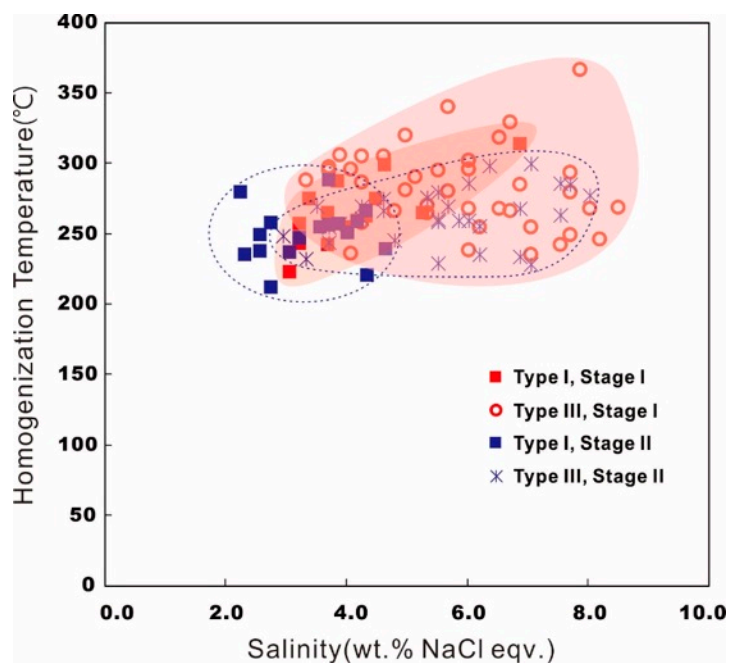


Figure 11. Plot of salinity vs. homogeneous temperature for fluid inclusions of different stages from the Koka deposit.

Moreover, varying degrees of CH₄ involvement in the fluid system were detected in the stage I FIs, and CH₄ may lead to fluid immiscibility of the NaCl–H₂O–CO₂ system at depth [34].

We calculated the densities of the type I (salinity <5 wt% NaCl eqv) and type II (CO₂-rich) inclusions in stage I via Flincor software [35] of 0.711–0.858 g/cm³ and 0.757–0.904 g/cm³, respectively, and then estimated the pressure in the range from 73 to 278 MPa, Figure 12 [11,36–38]). In addition, we can constrain the temperatures at ~290 °C from fluid inclusion microthermometry which is in agreement with the temperature obtained from sulfur isotope calculation of galena-sphalerite pair (see below). Then we obtained an estimated pressure between 106 and 168 MPa, which was similar to the estimated pressure between 105 and 250 MPa (Figure 13) using the method of Van den Kerhof and Thiéry [39]. Hence, we use 168 MPa to better constrain the estimated trapping pressure of stage I, corresponding to a maximum depth of 6.3 km (lithostatic pressure; rock density of 2.7 g/cm³).

(2) Stage II

The occurrence and composition of different FIs types suggest that the ore-forming fluid from stage II is a medium-temperature, low-salinity NaCl–H₂O–CO₂ fluid. The temperature of the ore-forming fluid decreased from stage I to II, most likely due to the progressive cooling of the fluid system or/and mixing with relatively low-T fluid, whereas the meteoric water mixing is supported by the results of the hydrogen and oxygen isotopes. In addition, the water content increased in the fluid of stage II, suggesting a water mixing. Salinity from stage I to II changed slightly, most likely due to the precipitation of metal elements in stage II.

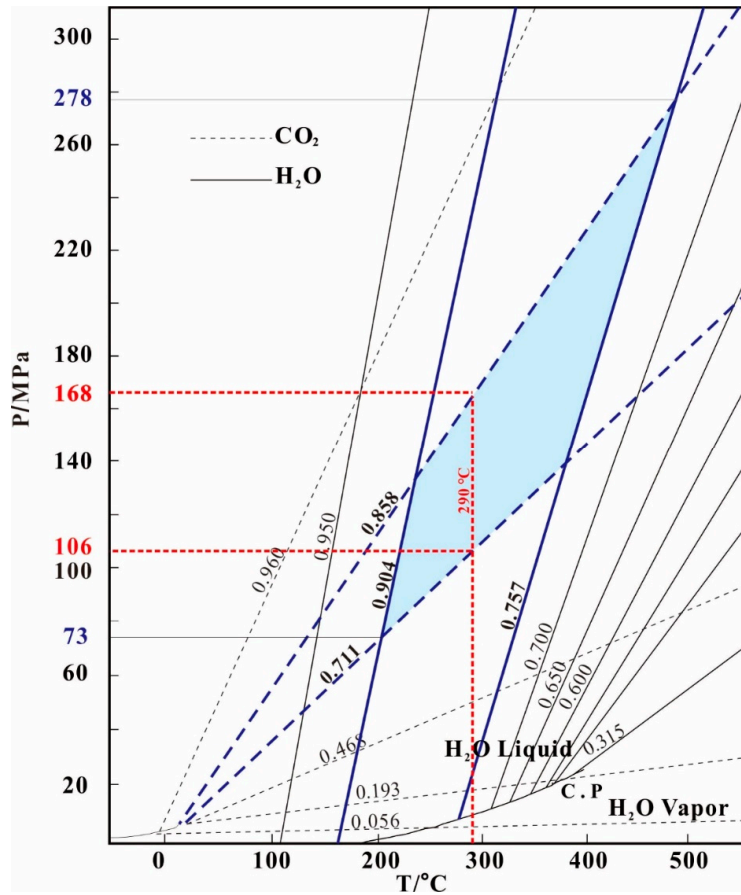


Figure 12. Pressure estimations for the primary fluid inclusions of the Koka deposit (after Roedder and Bodnar [36]).

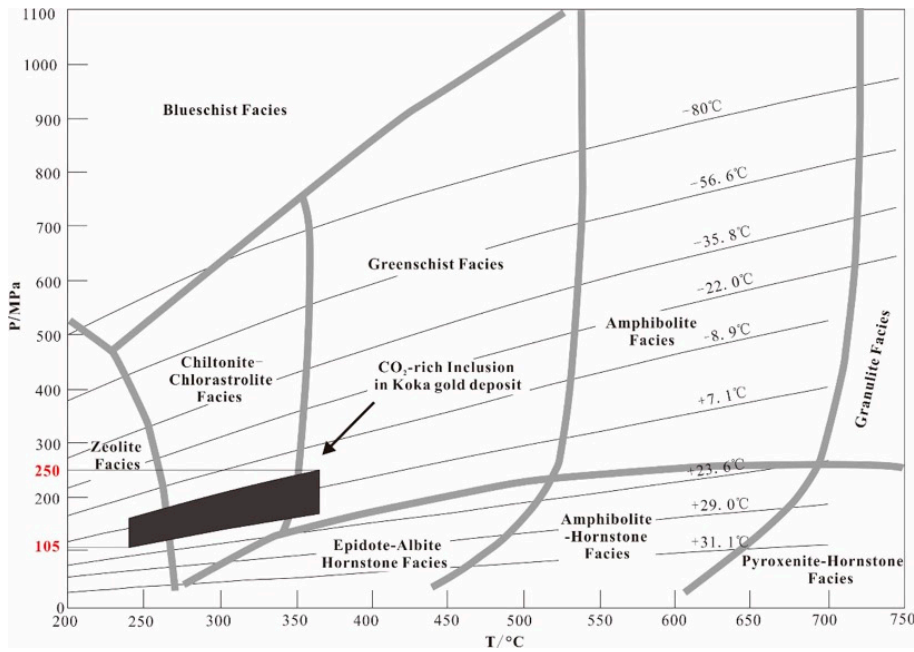


Figure 13. Pressure estimations for the primary fluid inclusions of the Koka deposit (after Van den Kerhof and Thiéry 2001 [39]).

7.2. Source of Ore-Forming Fluids and Metal

Most of the δD_{fluid} values (-57.0 to -50.1%) and the $\delta^{18}O_{\text{H}_2\text{O}}$ values ($+1.7$ to $+2.7\%$) of the ore quartz in the Koka gold deposit fell within the ranges of the isotopic compositions of metamorphic water [26,40], and near the primitive magmatic water field (Figure 9). The H–O data suggest that these ore-forming fluids were derived from metamorphic water, and that magmatic water could mix within the ore-forming fluids.

The $\delta^{13}C$ values of the quartz samples ranged from -5.5 to -4.4% , which were higher than those of the organic matter (averaging -25% [41]), CO_2 dissolved in water (-9 to -20% [42]), atmospheric CO_2 ($\sim -8\%$ [43] or -7 to -11% [42]), and crust (-7% [44]), and lower than the marine carbonates ($\sim 0\%$ [41]), but consistent with the C isotopic compositions of igneous/magma systems (-3 to -30% [42]; mantle (-5 to -7% [41]). In the $\delta^{13}C$ vs. $\delta^{18}O$ diagram, all of the quartz samples were plotted within the granite box field (Figure 8), indicating that carbon in the early ore-forming fluids was likely to be provided by magmatic water. Moreover, the late stage quartz samples showed an obvious trend of influence by low temperature alteration, which suggests a temperature cooling in the late ore-forming system. This interpretation is consistent with the results of the fluid inclusion microthermometry.

The $\delta^{34}S$ values of sulfides in the Koka gold deposit exhibited a narrow range of values that were close to 0% (-1.3 to $+2.7\%$, Figure 10), which suggests that the sulfides that precipitated from the fluid system originated from a single sulfur source that was primarily comprised of deep-seated magma ($\delta^{34}S = 0 \pm 3\%$ [45,46]). Moreover, the $\delta^{34}S$ values exhibited a trend of $\delta^{34}S_{\text{pyrite}} > \delta^{34}S_{\text{sphalerite}} > \delta^{34}S_{\text{galena}}$, which is consistent with the crystallization sequence of minerals in a hydrothermal system under the conditions of sulfur isotopic fractionation equilibrium [45,47]. These data suggest that the hydrothermal system reached a state of sulfur isotopic fractionation equilibrium before its ore minerals were precipitated [48–50], suggesting that these ore-forming materials were predominantly sourced from magma. Then we calculated the galena-sphalerite pair and obtained a temperature of 265 ± 19 °C according to Ohmoto and Rye 1979 [45], which is in agreement with the temperatures obtained from oxygen isotopes.

7.3. Genetic Model for Ore Deposition

The continental collision of East and West Gondwana caused the reconstruction of the regional juvenile crust and lithosphere, and the formation of East African Orogenic Belt (EAOB) during the Neoproterozoic (~ 650 Ma). Most of the juvenile crust were conjoined along the arc–arc suture, and the subsequent orogeny lasted nearly 100 Ma [15]. Due to the rapid convergence between East Gondwana and West Gondwana, the Eritrea region in the southern part of the EAOB experienced regional metamorphism [51].

^{40}Ar – ^{39}Ar ages of sericite in the gold-bearing quartz veins of the Koka deposit were 600–580 Ma (unpub. data), suggesting that the Koka deposit most likely formed in the Neoproterozoic. Moreover, several gold deposits in the Nubian Shield were reported to have formed at this period such as Sukhaybarat [52], An Najadi [53], Ad Duwayhi [54], and Lega-Dembi [55]. Regionally, Post orogenic a-type granite was formed after 610 Ma [15], combined with the formation age of Kyanite schist (U–Pb age of monazite, 593 ± 5 Ma [56]), suggesting that the time interval of 600–580 Ma was in the transition environment from crust compression to extension during the collision, accompanied by regional metamorphism.

The characteristics of geotectonic environment, occurrence of orebodies, mineral assemblages, and ore-forming fluid of the Koka gold deposit were similar to the features of orogenic gold deposits [11,30,57], whereas the carbon and sulfur isotopes suggested an igneous origin. Hence, the Koka gold deposit could be an orogenic gold deposit related to magmatism. The detailed ore-forming process is described as follows:

After the solidification of Koka granite, multi-fractures that existed in the granite became a relatively low-pressure zone in the district. Ore-bearing fluid, which was derived from the metamorphic strata and containing abundant CO_2 in high-pressure conditions, was driven by regional

thermodynamic processes to flow into the fault system of Koka granite. The temperature and pressure decreased as the ore-forming fluid rose during stage I, which led to CO₂ separating from the fluid accompanied by fluid immiscibility, leading to the dissolution of the Au-bearing complexes and a pH change in the residual fluid. Then, ore-forming ions such as Au⁺, Fe²⁺, Cu²⁺, Pb²⁺, Zn²⁺, and S²⁻ were precipitated at locations with advantageous structural conditions. During stage II, meteoric water was mixed in and cooled the fluid system, so that metal cations such as Fe²⁺ and S²⁻ remaining in the fluid were deposited in the structural fractures and micro-fractures of the existing veins.

8. Conclusions

(1) The ore-forming fluid of the Koka gold deposit is a medium- to low-temperature and low-salinity CO₂–NaCl–H₂O system, and ore-forming mechanisms include fluid immiscibility during an early stage and fluid mixing with meteoric water in subsequent stages at lower temperature. We used two methods to estimate a similar pressure at ~168 MPa, which corresponded to a depth of 6.3 km.

(2) The C–H–O isotopic compositions indicated that the ore-forming fluids of the Koka deposit could have originated from metamorphic strata and were likely to have made a considerable magmatic contribution. The S isotopic result suggest that the metals were derived from magma.

(3) Features of geology and ore-forming fluid at the Koka gold deposit were similar to those of orogenic gold deposits. Hence, the Koka deposit might be an orogenic gold deposit related to granite.

Author Contributions: K.Z., H.Y, J.W. and Y.-Q.X. conceived and designed the experiments; G.F.G., and W.X. performed the experiments; all authors wrote the paper.

Funding: This research was funded by (China Geological Survey, Mineral resources assessment of Egypt and adjacent areas) grant number (DD20160109), (the National Natural Science Foundation of China Project) grant number (41803044) and (the Construction Project of National Technical Standard System of Mineral Resources and Reserves) grant number (CB2017-4-10; 2017TP1029).

Acknowledgments: This work was supported by the China Geological Survey, Mineral resources assessment of Egypt and adjacent areas (DD20160109), Evaluation of large copper and gold resource bases in North Africa Project, and the National Natural Science Foundation of China Project (grant number 41803044).

Conflicts of Interest: The authors declare no conflict of interest.

References

1. Kröner, A.; Eyal, M.; Eyal, Y. Early Pan-African evolution of the basement around Elat, Israel and the Sinai Peninsula revealed by single-zircon evaporation dating and implication for crustal accretion rates. *Geology* **1990**, *18*, 545–548. [[CrossRef](#)]
2. Stern, R.J. Neoproterozoic (900–550 ma) arc assembly and continental collision in the east Africa orogen: Implications for the consolidation of Gondwanaland. *Annu. Rev. Earth & Planet. Sci.* **1994**, *22*, 319–351.
3. Stern, R.J. Neoproterozoic crustal growth: The solid Earth system during a critical episode of Earth history. *Gondwana Res.* **2008**, *14*, 33–50. [[CrossRef](#)]
4. Johnson, P.R.; Zoheir, B.A.; Ghebreab, W.; Stern, R.J.; Barrie, C.T.; Hamer, R.D. Gold-bearing volcanogenic massive sulfides and orogenic-gold deposits in the Nubian Shield. *S. Afr. J. Geol.* **2017**, *120*, 63–76. [[CrossRef](#)]
5. Ghebreab, W.; Greiling, R.O.; Solomon, S. Structural setting of Neoproterozoic mineralization, Asmara district, Eritrea. *J. Afr. Earth Sci.* **2009**, *55*, 219–235. [[CrossRef](#)]
6. Barrie, C.T.; Nielsen, F.W.; Aussant, C.H. The Bisha volcanic-associated massive sulfide deposit, western Nakfa terrane, Eritrea. *Econ. Geol.* **2007**, *102*, 717–738. [[CrossRef](#)]
7. Zhao, X.Z.; Duan, H.C.; Wang, F.X. General characteristics of geology and mineral resources in Eritrea and exploration progress. *Miner. Explor.* **2012**, *5*, 707–714. (In Chinese)
8. Xiang, P.; Wang, J.X. Ore geology character and type of Koka gold deposit, Eritrea. *Acta Mineral. Sin.* **2013**, *s2*, 1067–1068. (In Chinese)
9. Goldfarb, R.J.; Groves, D.I.; Gardoll, S. Orogenic gold and geologic time: A global synthesis. *Ore Geol. Rev.* **2001**, *18*, 12–75. [[CrossRef](#)]

10. Groves, D.I.; Goldfarb, R.J.; Robert, F. Gold deposits in metamorphic belts: Overview of current understanding, outstanding problems, future research, and exploration significance. *Econ. Geol.* **2003**, *98*, 1–29.
11. Goldfarb, R.J.; Groves, D.I. Orogenic gold: Common or evolving fluid and metal sources through time. *Lithos.* **2015**, *233*, 2–26. [[CrossRef](#)]
12. Abdelsalam, M.; Stern, R. Sutures and shear zones in the Arabian-Nubian Shield. *J. Afr. Earth Sci.* **1996**, *23*, 289–310. [[CrossRef](#)]
13. Stern, R.J.; Johnson, P.R.; Kröner, A.; Yibas, B. Neoproterozoic ophiolites of the Arabian-Nubian shield. *Dev. Precambrian Geol.* **2004**, *13*, 95–128.
14. Johnson, P.R.; Woldehaimanot, B. *Development of the Arabian–Nubian Shield: Perspectives on Accretion and Deformation in the Northern East African Orogen and the Assembly of Gondwana*; Special Publication: London, UK, 2003; pp. 290–325.
15. Johnson, P.R.; Andresen, A.; Collins, A.S.; Fowler, A.R.; Fritz, H.; Ghebreab, W.; Kusky, T.; Stern, R.J. Late Cryogenian–Ediacaran history of the Arabian–Nubian shield: A review of depositional, plutonic, structural, and tectonic events in the closing stages of the northern East African Orogen. *J. Afr. Earth Sci.* **2011**, *61*, 167–232. [[CrossRef](#)]
16. Drury, S.A.; Berhe, S.M. Accretion tectonics in Northern Eritrea revealed by remotely sensed imagery. *Geol. Mag.* **1993**, *130*, 177–190. [[CrossRef](#)]
17. Teklay, M. *Petrology, Geochemistry and Geochronology of Neoproterozoic Magmatic Arc Rocks from Eritrea: Implications for Crustal Evolution in the Southern Nubian Shield*; Department of Mines-Ministry of Energy Mines and Water Resources-State of Eritrea: Asmara, Eritrea, 1997; Volume 1, pp. 1–125.
18. Drury, S.A.; De Souza Filho, C.R. Neoproterozoic terrane assemblages in Eritrea: Review and prospects. *J. Afr. Earth Sci.* **1998**, *27*, 331–348. [[CrossRef](#)]
19. Zhao, K.; Yao, H.Z.; Wang, J.X.; Ghebsha, F.G.; Xiang, W.S.; Yang, Z. Zircon U-Pb geochronology and geochemistry of Koka granite and its geological significances, Eritrea. *Earth Sci.* in press. (In Chinese)
20. Dean, C.; David, L.; David, G. *Technical Report on the Koka Gold Deposit, Eritea*; Chalice Gold Mine Limited: Asmara, Eritrea, 2010; pp. 1–111.
21. Bozzo, A.T.; Chen, H.S.; Kass, J.R.; Barduhn, A.J. The properties of the hydrates of chlorine and carbon dioxide. *Desalination* **1975**, *16*, 303–320. [[CrossRef](#)]
22. Lu, H.Z.; Fan, H.R.; Ni, P.; Ou, G.X.; Shen, K.; Zhang, W.H. *Fluid Inclusions*; Science Press: Beijing, China, 2004; pp. 406–419. (In Chinese)
23. Clayton, J.; Tretiak, D.N. Amine-citrate buffers for pH control in starch gel electrophoresis. *J. Fish. Board Can.* **1972**, *29*, 1169–1172. [[CrossRef](#)]
24. Roedder, E. *Fluid Inclusions. Review in Mineralogy*; Mineralogical Society of America: Chantilly, VA, USA, 1984; pp. 1–644.
25. Chen, H.Y.; Chen, Y.J.; Baker, M.J. Evolution of ore-forming fluids in the Sawayaerdun gold deposit in the Southwestern Chinese Tianshan metallogenic belt. *J. Asian Earth Sci.* **2012**, *49*, 131–144. [[CrossRef](#)]
26. Taylor, H.P. The application of oxygen and hydrogen isotope studies to problems of hydrothermal alteration and ore deposition. *Econ. Geol.* **1974**, *69*, 843–883. [[CrossRef](#)]
27. Yang, L.Q.; Deng, J.; Guo, L.N.; Wang, Z.L.; Li, X.Z.; Li, J.L. Origin and evolution of ore fluid, and gold-deposition processes at the giant Taishang gold deposit, Jiaodong Peninsula, eastern China. *Ore Geol. Rev.* **2016**, *72*, 585–602. [[CrossRef](#)]
28. Yang, L.Q.; Guo, L.N.; Wang, Z.L.; Zhao, R.X.; Song, M.C.; Zheng, X.L. Timing and mechanism of gold mineralization at the Wang’ershan gold deposit, Jiaodong Peninsula, eastern China. *Ore Geol. Rev.* **2017**, *88*, 491–510. [[CrossRef](#)]
29. Qiu, K.F.; Taylor, R.D.; Song, Y.H.; Yu, H.C.; Song, K.R.; Li, N. Geologic and geochemical insights into the formation of the Taiyangshan porphyry copper–molybdenum deposit, Western Qinling Orogenic Belt, China. *Gondwana Res.* **2016**, *35*, 40–58. [[CrossRef](#)]
30. Yang, L.Q.; Deng, J.; Wang, Z.L.; Guo, L.N.; Li, R.H.; Groves, D.I.; Danyushevsky, L.V.; Zhang, C.; Zheng, X.L.; Zhao, H. Relationships between gold and pyrite at the Xincheng gold deposit, Jiaodong Peninsula, China: Implications for gold source and deposition in a brittle epizonal environment. *Econ. Geol.* **2016**, *111*, 105–126. [[CrossRef](#)]

31. Yang, L.Q.; Deng, J.; Li, R.P.; Guo, L.N.; Wang, Z.L.; Chen, B.H.; Wang, X.D. World-class Xincheng gold deposit: An example from the giant Jiaodong gold province. *Geosci. Front.* **2016**, *7*, 419–430. [[CrossRef](#)]
32. Groves, D.I.; Goldfarb, R.J.; Gebre-Mariam, M.; Hagemann, S.G.; Robert, F. Orogenic gold deposits: A proposed classification in the context of their crustal distribution and relationship to other gold deposit types. *Ore Geol. Rev.* **1998**, *13*, 7–27. [[CrossRef](#)]
33. Shepherd, T.J.; Rankin, A.H.; Alderton, D.H.M. *A Practical Guide to Fluid Inclusion Studies*; Chapman & Hall: Abingdon, UK, 1985; pp. 1–239.
34. Naden, J.; Shepherd, T.J. Role of methane and carbon dioxide in gold deposition. *Nature* **1989**, *342*, 793–795. [[CrossRef](#)]
35. Brown, P.E. FLINCOR: A microcomputer program for the reduction and investigation of fluid-inclusion data. *Am. Mineral.* **1989**, *74*, 1390–1393.
36. Roedder, E.; Bodnar, R.J. Geologic pressure determinations from fluid inclusion studies. *Annu. Rev. Earth Planet. Sci.* **1980**, *8*, 263–301. [[CrossRef](#)]
37. Xiong, Y.Q.; Shao, Y.J.; Zhou, H.D.; Wu, Q.H.; Liu, J.P.; Wei, H.T.; Zhao, R.C.; Cao, J.Y. Ore-forming mechanism of quartz-vein-type W-Sn deposits of the Xitian district in SE China: Implications from the trace element analysis of wolframite and investigation of fluid inclusions. *Ore Geol. Rev.* **2017**, *83*, 152–173. [[CrossRef](#)]
38. Xiong, S.; He, M.; Yao, S.; Cui, Y.; Shi, G.; Ding, Z.; Hu, X. Fluid evolution of the Chalukou giant Mo deposit in the northern Great Xing'an Range, NE China. *Geol. J.* **2015**, *50*, 720–738. [[CrossRef](#)]
39. Van den Kerkhof, A.; Thiéry, R. Carbonic inclusions. *Lithos* **2001**, *55*, 49–68. [[CrossRef](#)]
40. Qiu, K.F.; Marsh, E.; Yu, H.C.; Pfaff, K.; Gulbransen, C.; Gou, Z.Y.; Li, N. Fluid and metal sources of the Wenquan porphyry molybdenum deposit, Western Qinling, NW China. *Ore Geol. Rev.* **2017**, *86*, 459–473. [[CrossRef](#)]
41. Hoefs, J. *Stable Isotope Geochemistry*, 6th ed.; Springer: Berlin/Heidelberg, Germany, 2009; pp. 130–135.
42. Hoefs, J. *Stable Isotope Geochemistry*, 3rd ed.; Springer: Berlin/Heidelberg, Germany, 1997; pp. 1–201.
43. Schidowski, M.; Hayes, J.M.; Kaplan, I.R. Isotopic inferences of ancient biochemistry: Carbon, sulfur, hydrogen and nitrogen. In *Earth's Earliest Biosphere*; Schopf, J.W., Ed.; Princeton University Press: Princeton, NJ, USA, 1983; pp. 149–186.
44. Faure, G. *Principles of Isotope Geology*, 2nd ed.; Wiley: New York, NY, USA, 1977; p. 589.
45. Ohmoto, H.; Rye, R.O. Isotopes of sulfur and carbon. In *Geochemistry of Hydrothermal Ore Deposits*, 2nd ed.; Barnes, H.L., Ed.; John Wiley and Sons: New York, NY, USA, 1979; pp. 509–567.
46. Chaussidon, M.; Lorand, J.P. Sulphur isotope composition of orogenic spinel lherzolite massifs from Ariege (North-Eastern Pyrenees, France): An ion microprobe study. *Geochim. Cosmochim. Acta.* **1990**, *54*, 2835–2846. [[CrossRef](#)]
47. Xiong, Y.Q.; Shao, Y.J.; Mao, J.W.; Wu, S.C.; Zhou, H.D.; Zheng, M.H. The polymetallic magmatic-hydrothermal Xiangdong and Dalong systems in the W-Sn-Cu-Pb-Zn-Ag Dengfuxian orefield, SE China: Constraints from geology, fluid inclusions, H-O-S-Pb isotopes, and sphalerite Rb-Sr geochronology. *Miner. Depos.* **2019**. [[CrossRef](#)]
48. Zheng, Y.F.; Xu, B.L.; Zhou, G.T. Geochemical studies of stable isotopes in minerals. *Earth Sci. Front.* **2000**, *7*, 299–320. (In Chinese)
49. Deng, J.; Liu, X.F.; Wang, Q.F.; Pan, R.G. Origin of the Jiaodong-type Xinli gold deposit, Jiaodong peninsula, China: Constraints from fluid inclusion and C-D-O-S-Sr isotope compositions. *Ore Geol. Rev.* **2015**, *65*, 674–686. [[CrossRef](#)]
50. Yang, L.Q.; Deng, J.; Li, N.; Zhang, C.; Yu, J.Y. Isotopic characteristics of gold deposits in the Yangshan Gold Belt, West Qinling, central China: Implications for fluid and metal sources and ore genesis. *J. Geochem. Explor.* **2016**, *168*, 103–118. [[CrossRef](#)]
51. Ghebream, W. Tectono-metamorphic history of Neoproterozoic rocks in eastern Eritrea. *Precambrian Res.* **1999**, *98*, 83–105. [[CrossRef](#)]
52. Albino, G.V.; Jalal, S.; Christensen, K. Neoproterozoic mesothermal gold mineralization at Sukhaybarat East mine. *Trans. Inst. Min. Metall. (Sect. B Appl. Earth Sci.)* **1995**, *104*, 157–170.
53. Walker, B.M.; Lewis, R.S.; Al Otaibi, R.; Ben Talib, M.; Christian, R.; Gabriel, B.R. *An Najadi Gold Prospect, Kingdom of Saudi Arabia*; Geology and Gold-Resource Assessment; Saudi Arabian Deputy Ministry for Mineral Resources Technical Report, USGS-TR-94-5; Reston Publishing Service Center: Reston, VA, USA, 1994; pp. 1–89.

54. Doebrich, J.L.; Zahony, S.G.; Leavitt, J.D.; Portacio, J.S., Jr.; Siddiqui, A.A.; Wooden, J.L.; Fleck, R.J.; Stein, H.J. Ad Duwayhi, Saudi Arabia: Geology and geochronology of a Neoproterozoic intrusion-related gold system in the Arabian shield. *Econ. Geol.* **2004**, *99*, 713–741. [[CrossRef](#)]
55. Billay, A.Y.; Kisters, A.F.M.; Meyer, F.M.; Schneider, J. The geology of the Lega Dembi gold deposit, southern Ethiopia: Implications for Pan-African gold exploration. *Miner. Depos.* **1997**, *32*, 491–504. [[CrossRef](#)]
56. Andersson, U.B.; Ghebreab, W.; Teklay, M. Crustal evolution and metamorphism in east-central Eritrea, south-east Arabian-Nubian Shield. *J. Afr. Earth Sci.* **2006**, *44*, 45–65. [[CrossRef](#)]
57. Chen, Y.J.; Ni, P.; Fan, H.R.; Prajno, F.; Nai, Y.; Su, W.C.; Zhang, H. Diagnostic fluid inclusions of different types hydrothermal gold deposits. *Acta Petrol. Sin.* **2007**, *23*, 2085–2108. (In Chinese)



© 2019 by the authors. Licensee MDPI, Basel, Switzerland. This article is an open access article distributed under the terms and conditions of the Creative Commons Attribution (CC BY) license (<http://creativecommons.org/licenses/by/4.0/>).